

## THE MAXIMUM TORQUE OF SYNCHRONOUS AXIAL PERMANENT MAGNETIC COUPLINGS

U. Ausserlechner\*

Infineon Technologies Austria AG, Siemensstrasse 2, Villach 9500, Austria

**Abstract**—Axial permanent magnetic couplings are composed of two discs with a small air-gap in-between. Each disc consists of several segments in the shape of slices of cakes. The segments are polarized in axial direction with alternating polarity. In this work the homogeneous magnetization in the segments is replaced by equivalent currents on the surface of the segments (Amperean model). In a simplified model we consider only radial currents whereas azimuthal currents along the perimeter of the discs are discarded. This corresponds to the arrangement where one of the discs has much larger diameter than the other disc. Compared to the case of two equal discs it leads to a notable error in the magnetic field near the perimeter, yet it has only a small effect on the torque, especially for the case of optimum couplings. This trick allows for summing up the fields of all segments in closed form. A concise double integral over the radial magnetic field component describes the torque. An investigation of this integral reveals many properties of axial magnetic couplings: A diagram is introduced and areas in this diagram are identified where the torque shows overshoot, rectangular pulse shape or sinusoidal dependence versus twist angle between both discs. The diagram contains also a curve for maximum torque and one point on this curve is of considerable economic significance: It denotes the global maximum of torque over magnet mass.

---

*Received 15 February 2012, Accepted 21 March 2012, Scheduled 4 April 2012*

\* Corresponding author: Udo Ausserlechner (udo.ausserlechner@infineon.com).

## 1. INTRODUCTION

Axial permanent magnetic couplings transfer torque between two discs (or wide rings) facing each other. Each disc has a multitude of permanent magnetic segments, each segment having the shape of a piece of cake. Before the torque can be computed one has to compute the magnetic field generated by one of the two discs. This can be done in numerous ways [1–14]. In the majority of these publications the contributions of all segments are summed up numerically. Only [1, 9, 11, 12] present formulae where the summation was done in closed form. The torque computation means integrating over the force density of these fields. Without a closed solution for the magnetic field this leads to a large number of multiple integrals (in general up to six). Although this procedure renders numerical results [15–19] it seems difficult or even impossible to derive general conditions for torque maximization. Therefore experimental investigation is still important to study the various degrees of freedom in the design of these couplings [20–23].

This work is based on [1], where closed analytical formulae for the magnetic field components of axially magnetized multi-pole discs and rings are given. There also the torque of axial magnetic couplings is studied in the limit of infinitely thin discs. In this work we extend the discussion to discs of finite thickness. It leads to single and double integrals that cannot be solved in closed form. Yet a diagram is found that visualizes these integrals in a normalized way. Finally this diagram gives a guideline on how to optimize axial magnetic couplings.

## 2. DEFINITIONS

A cylindrical coordinate system  $(r, \psi, z)$  with unit vectors  $(\vec{n}_r, \vec{n}_\psi, \vec{n}_z)$  is used. The  $z$ -axis is the axis of rotation of both discs. Each disc is made up of  $2p$  segments, each covering an azimuthal angle

$$\psi_{k,1} \leq \psi \leq \psi_{k,3}, \quad 0 \leq k \leq 2p - 1, \quad (1a)$$

$$\psi_{k,1} = -\pi/(2p) + \pi k/p, \quad \psi_{k,3} = \pi/(2p) + \pi k/p \quad (1b)$$

The magnetization in the  $k$ -th segment is given by  $\vec{M}_k = (-1)^k (B_{\text{rem}}/\mu_0) \vec{n}_z$ . It has only a  $z$ -component and it is homogeneous inside each segment. In axial direction the lower disc extends from  $-t/2 \leq z \leq t/2$  and the upper disc extends from  $g+t/2 \leq z \leq g+3t/2$ , where  $g$  is the air-gap between both discs. Note that the term ‘‘axial magnetic coupling’’ refers to both the axial direction of magnetization and the axial shift in position between both discs. Examples are shown in Fig. 1.

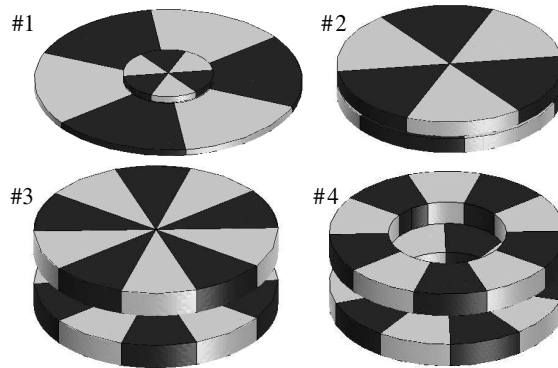


**Figure 1.** Several cases of axial magnetic couplings: Dark segments are magnetized upwards and light segments are magnetized downwards. Driving disc and driven disc have the same number of segments and the same thickness. #1 shows the most simple model of the presented theory, where the driving disc is infinitely large and the driven disc has a finite diameter  $2r_2$ . The spacing between the discs is arbitrary — both narrow and wide gaps are covered by the theory. Also the thickness and the number of poles is arbitrary. #2 shows a coupling with discs having identical diameters spaced apart by a narrow gap. #3 shows the same discs at wider gap and larger number of poles. #4 shows an arrangement where the discs of #3 have a bore with inner diameter  $2r_1 > 0$ . The presented theory is exact for #1, but it is only an approximation of #2, #3, and #4.

Let us call the lower disc *driving disc* and the upper disc *driven disc*. Although the roles of both discs could be exchanged, for the sake of clarity we stick to the notion that the driving disc is the source of a magnetic field into which the driven disc is immersed. Thus the two discs are assumed to interact only via linear superposition without any demagnetization effects of one disc on the other. Then the torque on the driven disc is the integral of radial distance times azimuthal component of force density subtending the volume of the driven disc

$$T (\text{on driven disc}) = \int_{\text{volume of driven disc}} r f_{\psi} dV \quad (2)$$

This azimuthal component of force density is given by (cf. Section 10 [1])

$$f_{\psi} = \frac{M_z (\text{of driven disc})}{r} \frac{\partial B_z (\text{of driving disc})}{\partial \psi} \quad (3)$$

To keep it simple both discs are supposed to have vanishing inner diameter ( $2r_1 = 0$ ). In practice the discs have a small bore yet its effect on the torque is negligible (see Subsection 3.2 and Fig. 5). The driven disc has outer diameter  $2r_2$ . Thus the integral in (2) extends in radial direction from  $r = 0$  to  $r = r_2$ . In practice the driving disc has the same outer diameter  $2r_2$ . The magnetic field of such a multi-polar disc of finite size leads to elliptic integrals that deny a closed summation formula over all  $p$  pole pairs. Yet in the sequel we need a closed summation formula to study the influence of  $p$  on the torque. Therefore we assume that the driving disc has infinite outer diameter, which allows for closed summation over all  $p$  pole pairs as shown in Section 6 of [1]. Of course this simplified model over-estimates the magnetic field and the torque. Yet we will show by comparison with finite element simulations that for reasonably small air-gap and thickness of discs or for large number of pole-pairs this error in torque is small. So the conceptual idea of our theory is to deliberately neglect a minor part of the magnetic field in order to get a better overview of the dominant mechanisms of torque transfer in axial magnetic couplings. The results of this theory assist in finding optimum configurations — in practice they should serve as starting point for more detailed numerical computations [24–29].

Within this model the torque can be expressed as a double integral over the  $z$ -component of the magnetic field (cf. (59) in [1])

$$T(\psi_0) = \frac{4pB_{\text{rem}}r_2^2}{\mu_0} \int_{\rho=0}^1 \int_{z=g+t/2}^{g+3t/2} B_z \left( r_2\rho, \psi_0 + \frac{\pi}{2p}, z \right) \rho d\rho dz \quad (4)$$

or as a single integral over the  $r$ -component of the magnetic field (cf. (62) in [1])

$$T(\psi_0) = \frac{2pB_{\text{rem}}r_2^3}{\mu_0} \int_{\rho=0}^1 (1 - \rho^2) \left\{ B_r \left( r_2\rho, \psi_0 + \frac{\pi}{2p}, g + \frac{3t}{2} \right) - B_r \left( r_2\rho, \psi_0 + \frac{\pi}{2p}, g + \frac{t}{2} \right) \right\} d\rho \quad (5)$$

where  $\psi_0$  specifies the angular shift between both discs. Equation (5) is better suited for our discussion: Shortcomings of our model with the infinitely large driving disc lead to significant errors in the  $B_r$ -field near  $r = r_2$ , however, in the integral they are strongly suppressed by the factor  $(1 - \rho^2)$ . This is the justification why our simplified model with infinitely large driving disc can be used for torque optimization.

### 3. THE RADIAL FIELD COMPONENT OF THE DRIVING DISC

#### 3.1. The Infinitely Large Driving Disc

For an infinitely large driving disc the field can be expressed as (see (30) in [1])

$$B_r(r, \psi, z) = \frac{-B_{\text{rem}}}{\pi} \int_{\beta=p \operatorname{arcsinh}((z-t/2)/r)}^{p \operatorname{arcsinh}((z+t/2)/r)} \frac{\cos(p\psi) \sinh(\beta/p) \cosh\beta}{(\cosh\beta)^2 - (\sin(p\psi))^2} d\beta \quad (6)$$

In the limit of vanishing thickness the properties of this field component were discussed in [1]. In a similar way they also hold for discs with finite thickness as explained in the following paragraph.

At large axial distance it holds  $p \operatorname{arcsinh}((z-t/2)/r) > 1$ . There the  $B_r(\psi)$ -pattern is sinusoidal. At small axial distance  $p(z-t/2) < r$  it shows overshoot. Conversely, at infinite radial distance the  $B_r(\psi)$ -pattern shows overshoot, and this overshoot is reduced as the test point approaches the axis. For small enough radial distance the overshoot disappears; then the pattern is pulse shaped and with even smaller radial distance it becomes sinusoidal. Thus, if the radius  $r_2$  of the driven disc is small enough it experiences no field with overshoot. In the following discussion we will see that for maximum torque overshoot has to be avoided. Therefore the overshoot is studied in more detail in Appendix A.

In the absence of overshoot the amplitude of the  $B_r(\psi)$ -pattern is

$$\hat{B}_r^{(\text{no})}(r, z) = B_r\left(r, \psi = \frac{\pi}{p}, z\right) = \frac{B_{\text{rem}}}{\pi} \int_{\beta=p \operatorname{arcsinh}((z-t/2)/r)}^{p \operatorname{arcsinh}((z+t/2)/r)} \frac{\sinh(\beta/p)}{\cosh\beta} d\beta \quad (7)$$

This non-overshoot amplitude is indicated by the index “(no)”. It diminishes like  $(r/|z|)^{p-1} / \sqrt{r^2 + z^2}$  near the axis. For large  $p$  this is the reason why the torque does not change notably if the driven disc has a bore.

At large radial distance the non-overshoot amplitude also diminishes (it decreases like  $r^{-2}$ ). Thus for  $p > 1$  there must be a maximum at intermediate radial distances<sup>†</sup>, which can be found by

<sup>†</sup> For  $p = 1$  the amplitude  $\hat{B}_r^{(\text{no})}$  does not vanish at  $r = 0$ : It has its maximum there and it decreases monotonically versus radial distance  $\hat{B}_r^{(\text{no})} = (B_{\text{rem}}/\pi) \ln(1 + t(2g+t)/(r^2 + g^2))$ .

differentiation  $\partial \hat{B}_r^{(\text{no})} / \partial r = 0$ . With  $z = t/2 + g$ ,  $\gamma = g/r$  and  $\tau = t/r$  this gives

$$\frac{\cosh(p \operatorname{arcsinh} \gamma)}{\cosh(p \operatorname{arcsinh}(\gamma + \tau))} \sqrt{\frac{1 + \gamma^2}{1 + (\gamma + \tau)^2}} = \frac{\gamma^2}{(\gamma + \tau)^2} \quad (8)$$

the solution of which is given in Table 1 and Fig. 2. Obviously for large torques  $r$  should be significantly lower than  $r_2$  so that the integrand in (5) is large.

### 3.2. The Driving Disc with Finite Diameter

A numerical simulation was carried out for the parameters  $t = 15$  mm,  $r_2 = 80$  mm,  $p = 5$ . Fig. 3 shows the geometry and the fluxlines, Fig. 4

**Table 1.** Solution of  $\partial \hat{B}_r^{(\text{no})} / \partial r = 0$ : The table gives values for  $\operatorname{parcsinh} \gamma$  for several values of  $\operatorname{parcsinh} \tau$  for the extreme values  $p = 2$  and  $p \rightarrow \infty$  (the solutions for all other  $p$  are between these two extremes). The case  $\operatorname{parcsinh} \tau = 0$  agrees with (28) in [1].

$\operatorname{parcsinh} \tau$	0.0	1.0	2.0	3.0	4.0
$p = 2$	1.94303	1.62785	1.32645	1.04252	0.799715
$p \rightarrow \infty$	2.06534	1.61003	1.23984	0.944123	0.710276

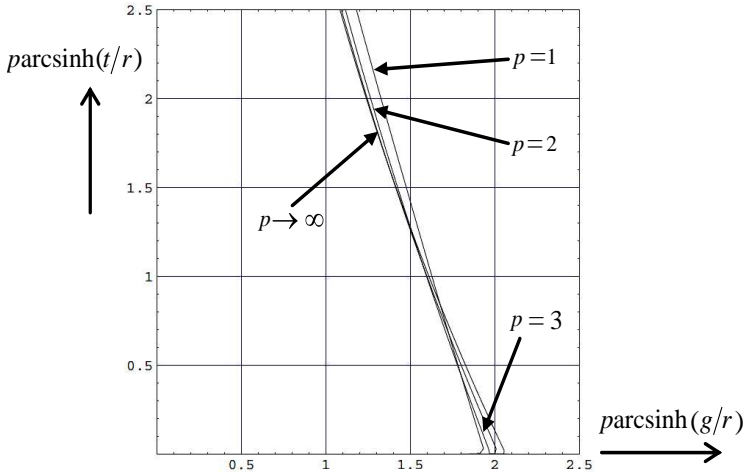


**Figure 2.** Solution of  $\partial \hat{B}_r^{(\text{no})} / \partial r = 0$  (cf. (8) and Table 1).

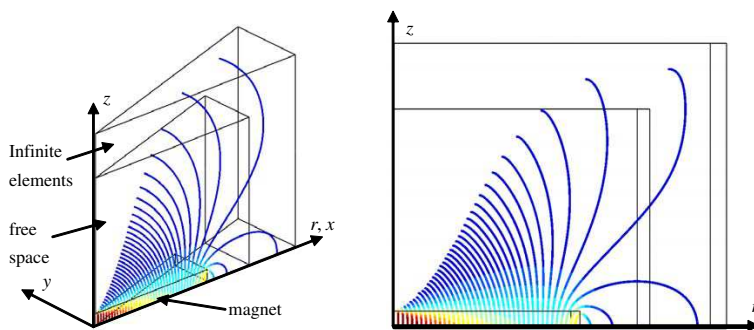


**Figure 3.** Fluxlines for a driving disc with 160 mm diameter, 15 mm thickness, having 5 pairs of north/south-poles. Due to symmetry only one quarter of the first magnetic pole  $k = 0$  with  $\vec{M}_k \cdot \vec{n}_z > 0$  is modeled (only half of the wedge and half of the thickness). The side view at the right hand side clearly shows that the flux lines bend towards the axis for  $r < 0.8 \times r_2$  whereas they bend outwards for  $r > 0.8 \times r_2$ .

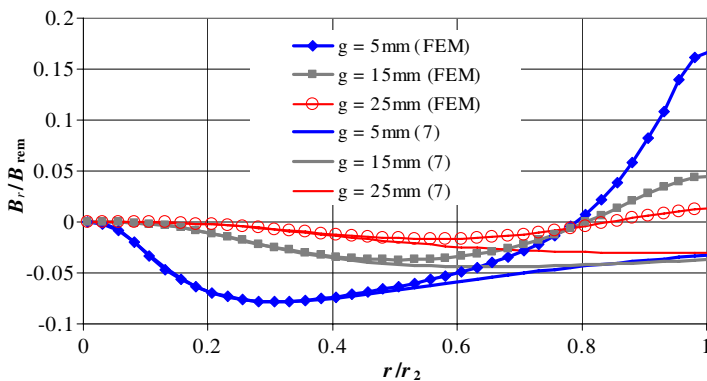


**Figure 4.** The radial field of the driving disc of Fig. 3 in  $y = 0$  at air-gaps 5, 15, 25 mm. This is identical to the non-overshoot amplitude  $\hat{B}_r^{(no)}(r, z)$  plotted versus radial distance. For small radial position the curves are accurately described by (7). Near the perimeter the finite element simulation (FEM) shows a large positive peak which (7) fails to describe.

shows the radial field component versus radial distance, and Fig. 5 shows the integrand of (5) versus radial distance. In Fig. 4 the magnetic field close to the perimeter of the disc differs drastically from the values obtained by (7), because the latter assumes an infinitely large disc. However, in Fig. 5 the integrand of (5) shows much smaller differences

between the finite disc (computed numerically) and the infinite disc (according to (6)). Fig. 5 is also interesting for small radial distance: There the integrand of (5) has large magnitude for small axial distance to the disc. This shows that for small number of pole-pairs, small air-gap between the two discs, and small thickness of the discs one cannot neglect the bore of the magnets, because the peak of the integrand occurs close to the axis.

The accuracy of the theory can be improved by the following approximation which includes effects of finite size of the driving disc. As shown in Fig. 6, we place a linear strip of alternating north- and south poles with width  $w$  next to a driving disc with radius  $r_2$  so that the strip touches the disc at its perimeter. The strip extends infinitely in  $x$ -direction. Its width should also go to infinity while its left edge remains unchanged. The length of magnetic poles of the strip should match the length of the segments on the perimeter  $2\pi r_2 = p\lambda$ . We want to improve the accuracy of the magnetic field calculation near the perimeter. In this region of interest the finite driving disc plus the strip cause a magnetic field that is similar to the field caused by an infinitely large driving disc. Of course this is only an approximation,

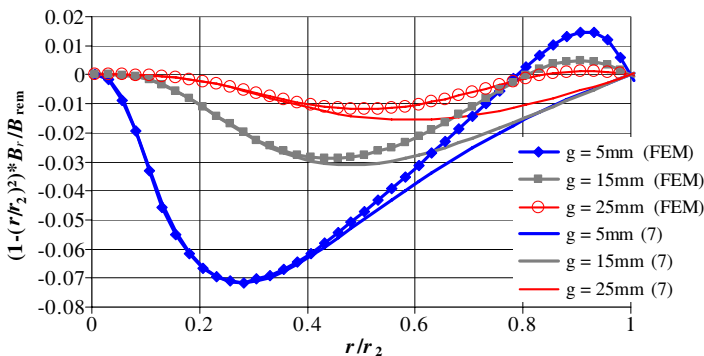


**Figure 5.** Integrand of the torque integral (5), where  $B_r$  is computed numerically with FEM or analytically with (7). The curves are plotted versus radial distance for the disc of Fig. 3 at air-gaps 5, 15, 25 mm. For small radial position both FEM simulation and (7) show good agreement. At larger radial distance (7) is less accurate. The torque is the area between these curves and the abscissa. The error due to the finite size of the driving disc has opposite sign than the main part of the integral: Thus neglecting these effects near the perimeter overestimates the torque. Note that for small distances  $g$  the integrand shows quite large peaks at small radial position. Therefore for small  $p$  and  $g$  the torque may still be affected by a bore in the magnet discs.

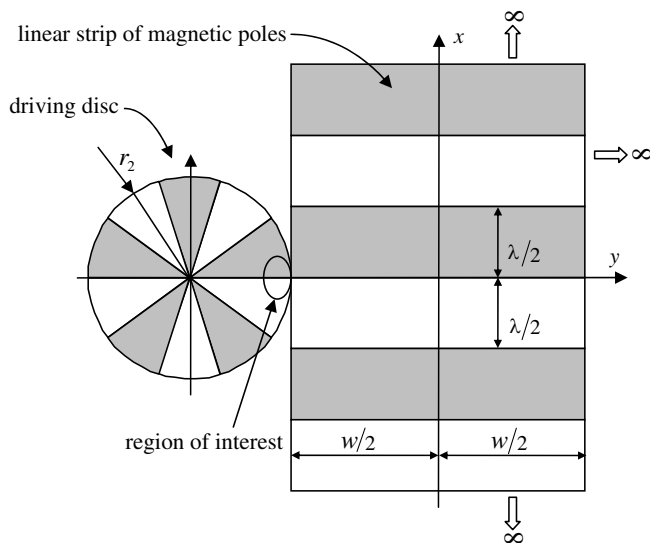


**Figure 6.** With regard to the field in the region of interest an infinitely large driving disc is equivalent to a finite disc plus an infinite strip where the lengths of the segments match  $2\pi r_2 = p\lambda$ . This is accurate for  $p \rightarrow \infty$  and for finite  $p$  it is an approximation.

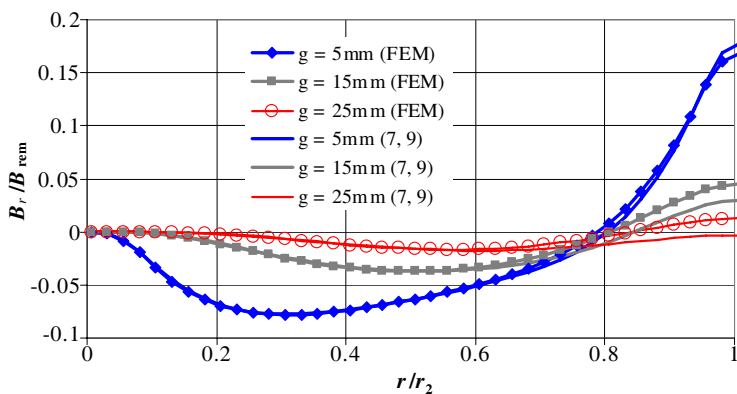


**Figure 7.** The same radial field as in Fig. 4, yet with strip correction term (9) subtracted from (7). For the sake of comparison the FEM results are also shown. At small air-gap (7, 9) is fairly accurate. At larger air-gap the relative error of (7, 9) is larger.

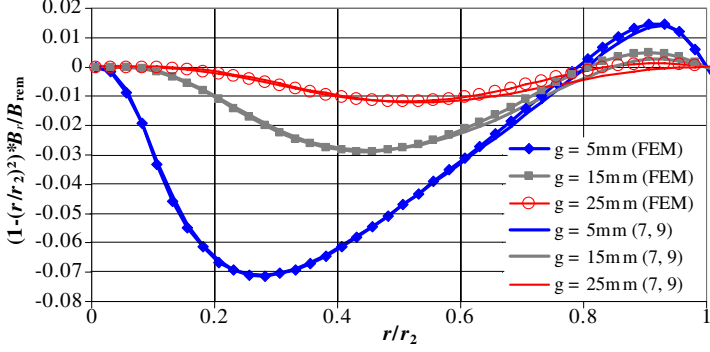


**Figure 8.** The same function as in Fig. 5, yet with strip correction term (9) subtracted from (7). FEM results are shown for comparison. A small error is visible at large radial distance. The integration over this function gives the torque and there the error is even smaller.

because it neglects the curvature beyond the disc perimeter. Yet in the limit of  $p \rightarrow \infty$  the aperture angle of each segment vanishes and hence the error of the approximation becomes negligible.

The  $B_y$ -field of the strip near its left edge can be computed by (51) of [1], if we set  $y = -w/2 - (r_2 - r)$  and  $x = r\psi$  and identify the  $B_y$ -field with the  $B_r$ -field

$$B_r = \frac{2B_{\text{rem}}}{\pi^2} \sum_{n=0}^{\infty} \frac{(-1)^n}{2n+1} \cos((2n+1)p\psi) \times K_0 \left( \frac{p}{r_2} (2n+1) \sqrt{\eta^2 + \zeta^2} \right) \Bigg|_{\eta=r-r_2-w}^{r-r_2} \Bigg|_{\zeta=z-t/2}^{z+t/2} \quad (9)$$

with the modified Bessel function  $K_0$ . In (9) we used the abbreviation  $f(x)|_{x=a}^b = f(b) - f(a)$ . Let  $w \rightarrow \infty$  and insert (9) into (5) to obtain the torque correction term from the strip

$$T_{\text{strip}}(\psi_0) \approx -p \left( \frac{2B_{\text{rem}}}{\pi} \right)^2 \frac{r_2^3}{\mu_0} \sum_{n=0}^{\infty} \frac{1}{2n+1} \sin((2n+1)p\psi_0) \times \int_{\rho=0}^1 (1-\rho^2) \left\{ K_0 \left( p(2n+1) \sqrt{(\rho-1)^2 + \gamma^2} \right) - 2K_0 \left( p(2n+1) \sqrt{(\rho-1)^2 + (\gamma+\tau)^2} \right) + K_0 \left( p(2n+1) \sqrt{(\rho-1)^2 + (\gamma+2\tau)^2} \right) \right\} d\rho \quad (10a)$$

The torque of the finite disc is approximately given by

$$T_{\text{finite disc}}(\psi_0) \approx T_{\text{infinite disc}}(\psi_0) - T_{\text{strip}}(\psi_0) \tag{10b}$$

As shown in Appendix B the correction term from the strip vanishes in the limit  $p \rightarrow \infty$ . Yet for finite  $p$  it improves the accuracy for torque computations significantly (Figs. 7 and 8).

#### 4. TORQUE OVERSHOOT

For the sake of simplicity we disregard the torque correction term from the strip (10a) in this section. It alters the results for finite  $p$  only slightly and makes no difference in the case  $p \rightarrow \infty$ . Inserting (6) into (5) gives the torque  $T$  versus angular twist  $\psi_0$  between driving disc and driven disc. At large air-gap  $g$  the  $B_r$ -field varies sinusoidally versus angular position  $\psi$  (cf. Appendix A). In this case, also the torque varies sinusoidally versus  $\psi_0$ . Yet at small air-gap the function  $T(\psi_0)$  becomes pulse shaped and at even smaller air-gaps it exhibits overshoot. In the limit of thin discs  $t \rightarrow 0$  this was discussed in Section 10 of [1]. Here we extend the discussion to discs with finite thickness  $t > 0$ .

Torque overshoot starts when the maxima of the pulses become flat, thus

$$\frac{\partial^2 T}{\partial \psi_0^2} = 0 \quad \text{for} \quad \psi_0 = \frac{-\pi}{2p} \tag{11}$$

With (5), (6), and (11) one arrives at an implicit equation for the so

**Table 2.** Numerical solution of (12) for  $p \operatorname{arcsinh} \gamma = 0$ : Torque overshoot limit curve for vanishing air-gap (cf. Fig. 9).

$p$	1	2	3	4	6	10	$\infty$
$p \operatorname{arcsinh} \tau$	0.834	0.743	0.718	0.708	0.700	0.696	0.694081

**Table 3.** Numerical solution of (12) for  $p \operatorname{arcsinh} \tau = 0$ : Torque overshoot limit curve for vanishing thickness of the multi-polar discs (cf. Fig. 9). The values agree with (72) in [1].

$p$	1	2	3	4	6	10	$\infty$
$p \operatorname{arcsinh} \gamma$	0.6197	0.5772	0.5659	0.5614	0.5581	0.5562	0.5552

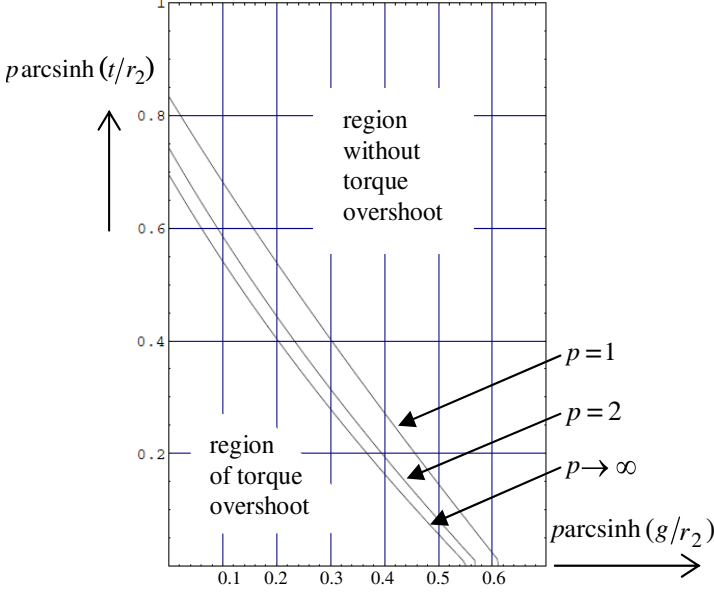


**Figure 9.** Torque overshoot limit curves (drawn for  $p = 1, 2, \infty$ ). Torque overshoot is confined to a small finite region in the  $(p \operatorname{arcsinh}\gamma; p \operatorname{arcsinh}\tau)$ -plane. See also numerical values in Tables 2 and 3.

called limit curve of torque overshoot

$$0 = \int_{\rho=0}^1 (1 - \rho^2) \left( \int_{\beta=p \operatorname{arcsinh}((\gamma+\tau)/\rho)}^{\operatorname{arcsinh}((\gamma+2\tau)/\rho)} \frac{3 - \cosh(2\beta)}{(\cosh\beta)^3} \sinh\left(\frac{\beta}{p}\right) d\beta - \int_{\beta=p \operatorname{arcsinh}(\gamma/\rho)}^{\operatorname{arcsinh}((\gamma+\tau)/\rho)} \frac{3 - \cosh(2\beta)}{(\cosh\beta)^3} \sinh\left(\frac{\beta}{p}\right) d\beta \right) d\rho \quad (12)$$

This limit curve separates the region where torque overshoot occurs from the region without torque overshoot in the  $(p \operatorname{arcsinh}\gamma; p \operatorname{arcsinh}\tau)$ -plane (see Fig. 9). Table 2 gives numerical values of  $p \operatorname{arcsinh}\tau$  at vanishing air-gap  $p \operatorname{arcsinh}\gamma$ . Table 3 gives numerical values of  $p \operatorname{arcsinh}\gamma$  at vanishing thickness of the discs  $p \operatorname{arcsinh}\tau = 0$ . Comparison of Fig. 9 with Fig. A1 in Appendix A shows that the region of torque overshoot is smaller than the region of overshoot in  $B_r$ - and  $B_z$ -fields. The reason is that torque is obtained by integrating

the fields over radial distance and there is no field overshoot at small radial distance.

In the limit  $p \rightarrow \infty$  we may skip the arcsinh-functions in (12). This is explained in Appendix C. Replacing  $\sinh(\beta/p) \rightarrow \beta/p$  and carrying out the inner integrals  $\int (3 - \cosh(2\beta)) (\cosh\beta)^{-3} \beta d\beta = 2(1 + \beta \tanh\beta) / \cosh\beta$  one obtains an equation that is better suited for numerical solution

$$\int_{\rho=0}^1 (1 - \rho^2) \left( \frac{1 + ((p\gamma + 2p\tau)/\rho) \tanh((p\gamma + 2p\tau)/\rho)}{\cosh((p\gamma + 2p\tau)/\rho)} + \frac{1 + (p\gamma/\rho) \tanh(p\gamma/\rho)}{\cosh(p\gamma/\rho)} - 2 \frac{1 + ((p\gamma + p\tau)/\rho) \tanh((p\gamma + p\tau)/\rho)}{\cosh((p\gamma + p\tau)/\rho)} \right) d\rho = 0 \quad (13)$$

In the limit  $p \operatorname{arcsinh}\tau \rightarrow p\tau \rightarrow 0$  we may develop (13) into a Mac Laurin series, with the dominant second order term. This leads to the solution  $p\gamma = 0.5552$  as in (72) of [1].

### 5. MAXIMUM TORQUE BY OPTIMUM NUMBER OF POLE-PAIRS

As shown in Section 10 of [1] highest torque values are obtained in the non-overshoot region. This torque amplitude is called pull-out torque and it is given by

$$\hat{T}^{(no)} = T \left( \psi_0 = \frac{-\pi}{2p} \right) = \frac{2pB_{rem}^2 r_2^3}{\mu_0 \pi} \int_{\rho=0}^1 (1 - \rho^2) \left( \int_{\beta=p \operatorname{arcsinh}(\gamma/\rho)}^{p \operatorname{arcsinh}((\gamma+\tau)/\rho)} \frac{\sinh(\beta/p)}{\cosh\beta} d\beta - \int_{\beta=p \operatorname{arcsinh}((\gamma+\tau)/\rho)}^{p \operatorname{arcsinh}((\gamma+2\tau)/\rho)} \frac{\sinh(\beta/p)}{\cosh\beta} d\beta \right) d\rho \quad (14)$$

The optimum number of pole-pairs is given by differentiating (14) against  $p$  and setting the result equal to zero. With  $\sinh(\beta/p) \rightarrow \beta/p$  for  $p \rightarrow \infty$  and Appendix C this leads to

$$\int_{\rho=0}^1 \left( \frac{1}{\rho^2} - 1 \right) \left\{ \frac{(p\gamma + 2p\tau)^2}{\cosh((\gamma + 2\tau)/\rho)} - 2 \frac{(p\gamma + p\tau)^2}{\cosh((\gamma + \tau)/\rho)} + \frac{(p\gamma)^2}{\cosh(p\gamma/\rho)} \right\} d\rho = 0 \quad (15)$$

This is an implicit equation for the optimum- $p$  curve in the  $(p \operatorname{arcsinh}\gamma; p \operatorname{arcsinh}\tau)$ -plane. It is shown in Fig. 10 and numerical values are given in Table 4.

The  $(p \operatorname{arcsinh} \gamma; p \operatorname{arcsinh} \tau)$ -diagram assists in getting a survey on how the four design parameters  $p$ ,  $g$ ,  $t$ , and  $r_2$  interact with the torque: If only the air-gap  $g$  is increased the point representing the system moves on a horizontal line to the right. If only the thickness  $t$  of the discs is increased it moves on a vertical axis upwards. If only the number of pole-pairs  $p$  is increased the point moves outwards on a straight line through the origin of the plane. If only the diameter of the discs is increased the point moves outwards on a curve that is a straight line going through the origin with some curvature at larger distance to the origin (only in the case  $g = t$  this curve is a perfectly straight line even at large distance from the origin).

Thus, if a typical coupling with  $g \ll r_2$  and  $t \ll r_2$  is designed, we may begin with  $p = 1$ . Then the point in the  $(p \operatorname{arcsinh} \gamma;$

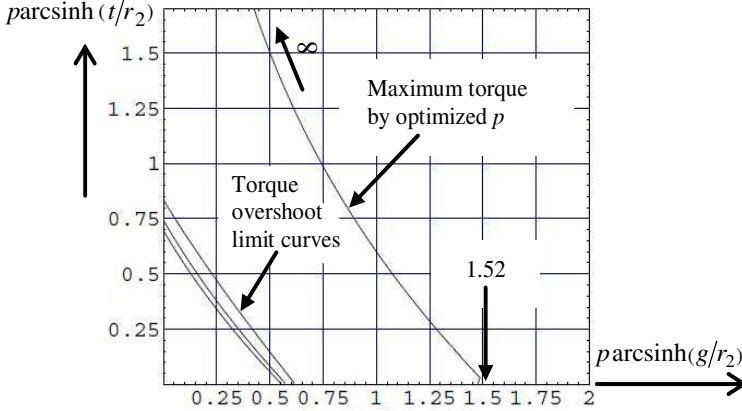


**Figure 10.** Root locus for axial magnetic couplings with maximized torque by optimum number of pole-pairs. This optimum- $p$  curve is shifted right of the torque overshoot limit curves (drawn for  $p = 1, 2, \infty$ ). See also numerical values in Table 4.

**Table 4.** Optimum- $p$  curve: Numerical solution of (15) (cf. Fig. 10). Bold numbers denote the most cost efficient design (cf. Section 6). The value  $p \operatorname{arcsinh} \gamma = 1.51812$  agrees with (79) in [1].

$p \operatorname{arcsinh} \gamma$	0	0.05679	0.14010	0.33224	0.50111	0.61142	0.74233
$p \operatorname{arcsinh} \tau$	$\infty$	4.0	3.0	2.0	1.5	1.25	1.0
$p \operatorname{arcsinh} \gamma$	<b>0.761740</b>	0.86359	1.00085	1.15519	1.32744	1.42046	1.51812
$p \operatorname{arcsinh} \tau$	<b>0.966215</b>	0.8	0.6	0.4	0.2	0.1	0

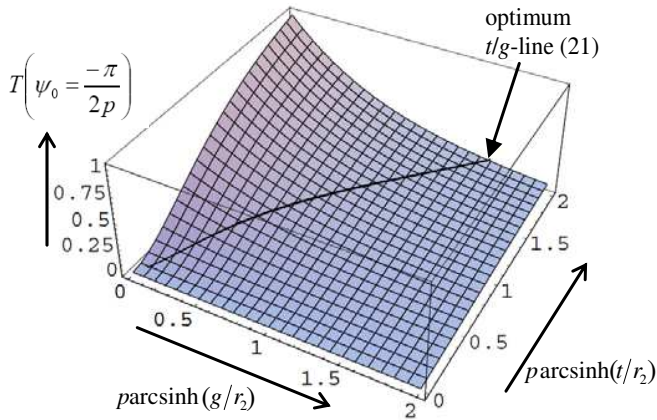


**Figure 11.** Torque amplitude (in units Newton-times-meter) of axial magnetic couplings without ferrous backplanes for  $2B_{rem}^2 r_2^3 / (\mu_0 \pi) = 1 \text{ Nm}$  and  $p \rightarrow \infty$  (non-overshoot case) according to (14). The torque for parameters along the line (21) is also drawn: It shows that the torque has a relative maximum if the point moves outwards along a straight line in the  $(p \arcsinh (g/r_2) ; p \arcsinh (t/r_2))$ -plane.

$p \arcsinh \tau$ )-plane is within the torque overshoot region. If we increase  $p$  the point moves outwards leaving the overshoot region: Then the  $T(\psi_0)$ -dependence is pulse shaped and with increasing  $p$  it resembles more and more a sine wave. During this outward movement of the point the peak torque value increases continuously until it reaches its maximum when the point traverses the optimum- $p$  curve. If  $p$  is increased beyond this value the torque decreases again.

Figure 11 shows the torque amplitude in a 3D-plot. It increases with smaller air-gap and thicker magnets, yet not infinitely. The maximum torque is obtained for vanishing air-gap and infinitely thick discs. For a finite air-gap  $g > 0$ , very thick discs, and large number of pole-pairs the torque amplitude tends to the limit

$$\lim_{p \rightarrow \infty} \lim_{\tau \rightarrow \infty} \hat{T}^{(no)} = \frac{2B_{rem}^2 r_2^3}{\mu_0 \pi} \int_{\rho=0}^1 (1 - \rho^2) \int_{\beta=p \arcsinh(\gamma/\rho)}^{\infty} \frac{\beta d\beta}{\cosh \beta} d\rho \quad (16a)$$

Reversing the sequence of inner and outer integration gives

$$\lim_{p \rightarrow \infty} \lim_{\tau \rightarrow \infty} \hat{T}^{(no)} = \frac{2B_{rem}^2 r_2^3}{\mu_0 \pi} \int_{\beta=p\gamma}^{\infty} \left( \frac{2\beta}{3} - p\gamma + \frac{(p\gamma)^3}{3\beta^2} \right) \frac{d\beta}{\cosh \beta} \quad (16b)$$

For small  $p\gamma$  we can develop (16b) into a Mac Laurin series. With

$$\begin{aligned} & \left. \frac{\partial}{\partial (p\gamma)} \int_{\beta=p\gamma}^{\infty} \left( \frac{2\beta}{3} - p\gamma + \frac{(p\gamma)^3}{3\beta^2} \right) \frac{d\beta}{\cosh\beta} \right|_{p\gamma \rightarrow 0} \\ &= - \int_{\beta=0}^{\infty} \frac{d\beta}{\cosh\beta} + \lim_{p\gamma \rightarrow 0} (p\gamma)^2 \int_{\beta=p\gamma}^{\infty} \frac{d\beta}{\beta^2 \cosh\beta} \end{aligned} \quad (16c)$$

With the rule of de l'Hospital one can prove that the second term is of type  $0 \times \infty$  and converges to zero. The first integral is equal to  $\pi/2$ . Thus the result for small air-gap is

$$\lim_{p \rightarrow \infty} \lim_{\tau \rightarrow \infty} \hat{T}^{(\text{no})} = \frac{2B_{\text{rem}}^2 r_2^3}{\mu_0 \pi} \left( \frac{4}{3} C_{\text{Catalan}} - \frac{\pi}{2} p\gamma + O^2(p\gamma) \right) \quad (17)$$

with Catalan's constant  $C_{\text{Catalan}} \cong 0.915966$ . For vanishing air-gap we get the absolute maximum torque

$$\hat{T}_{\text{max}} = \lim_{p \rightarrow \infty} \lim_{\tau \rightarrow \infty} \hat{T}^{(\text{no})} \Big|_{\gamma=0} = \frac{8B_{\text{rem}}^2 r_2^3}{3\mu_0 \pi} C_{\text{Catalan}} \cong 0.7775 \times \frac{B_{\text{rem}}^2 r_2^3}{\mu_0} \quad (18)$$

Thus with a strong anisotropic NdFeB magnet having  $B_{\text{rem}} = 1.32T$  one could theoretically obtain a torque of 135 Nm for discs with 10 cm diameter. Of course this is not practical, because the magnet mass would be huge and the air-gap needs to be kept close to zero. Yet according to (17) the decrease of torque at small air-gaps is only moderate:  $-13\%$  for  $pg/r_2 = 0.1$ .

## 6. MAXIMUM RATIO OF TORQUE OVER VOLUME OF MAGNET

In practice one wants to achieve a certain torque with minimum mass of magnet in order to keep the costs, the weight, and the inertia moment low. To this end we compute the ratio of torque amplitude over twice the volume of the driven disc  $V = 2\pi tr_2^2$  with Appendix C

$$\lim_{p \rightarrow \infty} \frac{\hat{T}^{(\text{no})}}{V} = \frac{B_{\text{rem}}^2 r_2}{\mu_0 \pi^2 g} \frac{p\gamma}{p\tau} \int_{\rho=0}^1 (1-\rho^2) \left( \int_{\beta=p\gamma/\rho}^{p(\gamma+\tau)/\rho} \frac{\beta d\beta}{\cosh\beta} - \int_{\beta=p(\gamma+\tau)/\rho}^{p(\gamma+2\tau)/\rho} \frac{\beta d\beta}{\cosh\beta} \right) d\rho \quad (19)$$

In (19) we factored out the term  $r_2/g$ :  $g$  is usually given by mechanical tolerances of the system and  $r_2$  is adjusted in order to achieve the

desired value of the torque. Fig. 12 shows that this ratio has a global maximum

$$\lim_{p \rightarrow \infty} \left( \frac{\hat{T}^{(no)}}{V} \right)_{\max} = 0.17854 \times \frac{B_{\text{rem}}^2 r_2}{\mu_0 \pi^2 g}. \quad (20a)$$

This maximum torque-volume ratio is obtained for

$$p \operatorname{arcsinh}(g/r_2) = 0.76174 \text{ and } p \operatorname{arcsinh}(t/r_2) = 0.966215. \quad (20b)$$

The ratio of the two coordinates in (20b) describes a straight line through the origin of the  $(p \operatorname{arcsinh} \gamma; p \operatorname{arcsinh} \tau)$ -diagram which we call optimum  $t/g$ -line

$$1.2684 = \frac{p \operatorname{arcsinh}(t/r_2)}{p \operatorname{arcsinh}(g/r_2)} \cong \frac{t}{g} \quad (21)$$

Thus for axial couplings the thickness of the magnets should be 27% larger than the spacing between them. Couplings with maximum torque-volume ratio must fulfill this geometrical requirement. From Section 5 we know that the point representing the coupling in the  $(p \operatorname{arcsinh} \gamma; p \operatorname{arcsinh} \tau)$ -diagram moves outwards on this straight line when  $p$  increases and there is a maximum torque when the line intersects the optimum- $p$  curve. This proves that the solution (20b) lies on the optimum- $p$  curve (cf. Fig. 13).

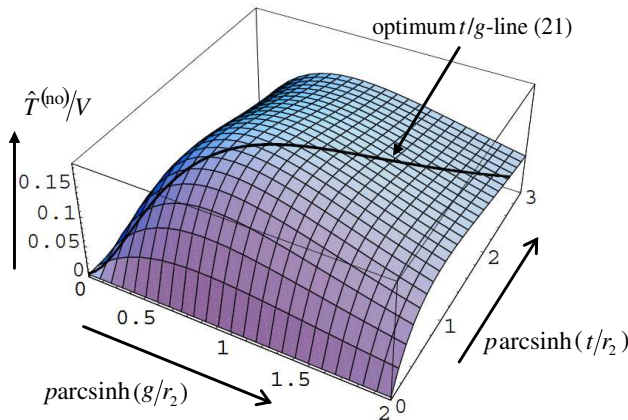


**Figure 12.** Torque-volume ratio (in units Newton-times-meter-per-cubic-meter): Ratio of non-overshoot torque amplitude over twice the volume of the driven disc for  $B_{\text{rem}}^2 r_2 / (\mu_0 \pi^2 g) = 1 \text{ Nm/m}^3$ . The maximum is  $0.17854 \text{ Nm/m}^3$ , it lies on the optimum  $t/g$ -line and occurs at  $p \operatorname{arcsinh}(g/r_2) = 0.76174$  and  $p \operatorname{arcsinh}(t/r_2) = 0.966215$ .

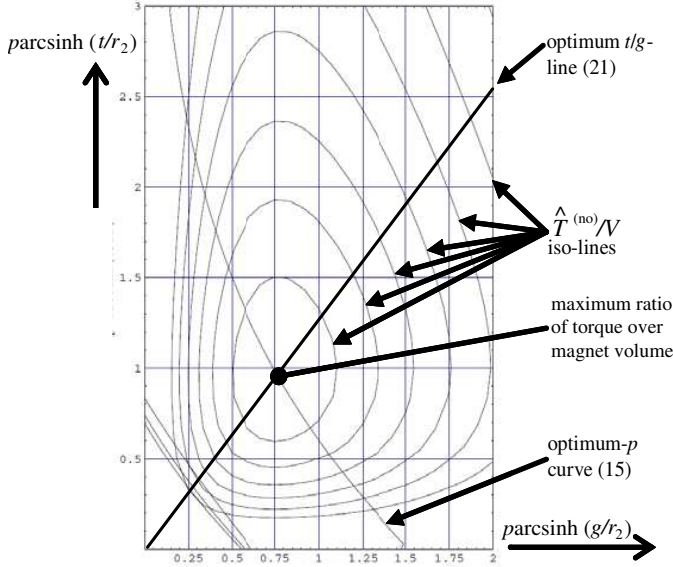


**Figure 13.** Torque-volume ratio in the  $(p \operatorname{arcsinh} \gamma; p \operatorname{arcsinh} \tau)$ -plane. The maximum torque-volume ratio is located on the crossing of the optimum  $t/g$ -line (21) with the optimum- $p$  curve (15).

With (21) and (20a) we get the most cost efficient torque

$$\hat{T}^{(\text{no})} \cong 0.144172 \times \frac{B_{\text{rem}}^2 r_2^3}{\mu_0} \quad \text{for}$$

$$t = r_2 \sinh \left( 1.2684 \times \operatorname{arcsinh} \frac{g}{r_2} \right) \quad \text{and} \quad p = \frac{0.76174}{\operatorname{arcsinh} (g/r_2)} \quad (22)$$

Comparison of (22) with (18) shows that the most cost efficient torque is 5.4 times smaller than  $\hat{T}_{\text{max}}$ . Therefore discs with 10 cm diameter and  $B_{\text{rem}} = 1.32T$  give cost efficient torques with 25 Nm. This holds for arbitrary air-gaps as long as (22) is fulfilled and the number of pole-pairs does not get too small. Theoretically a coupling with a 10 cm diameter and 1  $\mu\text{m}$  thick magnet and 0.79  $\mu\text{m}$  gap with 96423 pole pairs would also produce 25 Nm torque — thus one can minimize magnetic mass by improved accuracy in the spacing of the discs.

#### *Design Examples:*

Suppose a rare earth magnet with  $B_{\text{rem}} = 1.074T$ . A cost efficient coupling should be constructed that has 1000 Nm torque. With (22) it follows  $r_2 = 19.6$  cm. For this size an air-gap of approximately 1 cm

can be guaranteed by construction. With  $\text{parcsinh}(g/r_2) = 0.76174$ , we get  $p = 14.9$ . We choose  $p = 15$  and  $r_2 = 20$  cm. With  $\text{parcsinh}(t/r_2) = 0.966215$  we get  $t = 12.9$  mm. The volume of the driving disc is  $1621 \text{ cm}^3$ . With a mass density of  $7.5 \text{ g/cm}^3$  its mass is about  $12.2 \text{ kg}$ .

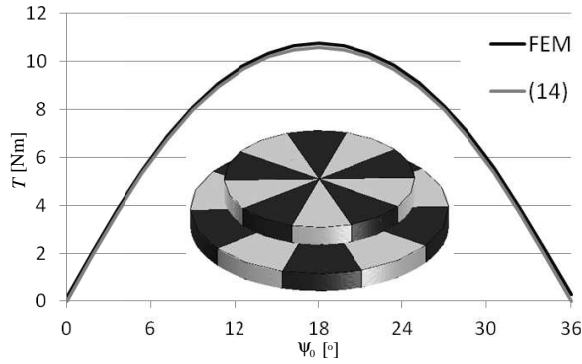


**Figure 14.** Comparison of torque: Finite element simulation (FEM) versus analytic formula (14). The coupling has the parameters  $B_{\text{rem}} = 0.54T$ ,  $g = 10$  mm,  $t = 13.5$  mm,  $p = 5$ ,  $r_2 = 67$  mm. The analytic formula (14) assumes infinitely large driving disc. The FEM model uses a driving disc which is 35% larger than the driven disc (see inset). For large driving discs the analytic formula (14) is perfectly accurate.

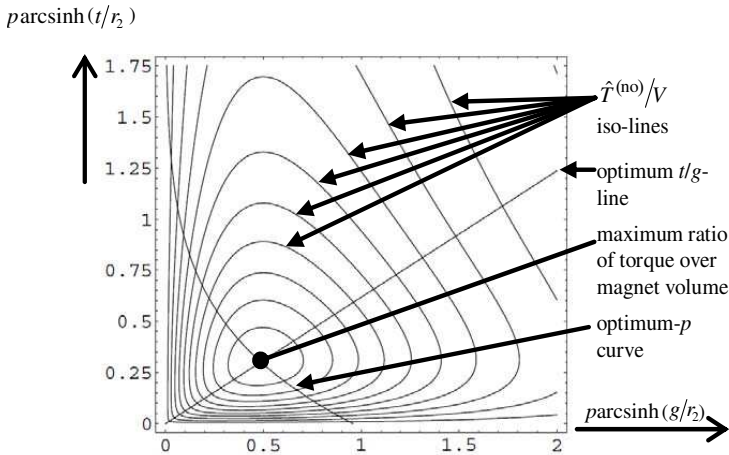


**Figure 15.** Torque-volume ratio, optimum- $p$  curve, and optimum  $t/g$ -line for axial magnetic couplings with two ferrous backplanes (derived from (25) in [30]).

Another coupling has  $B_{\text{rem}} = 0.54T$ ,  $g = 10$  mm,  $t = 13.5$  mm,  $p = 5$ , and  $r_2 = 67$  mm. It is close to the torque-volume maximum:  $p \operatorname{arcsinh}(g/r_2) = 0.744$ ,  $p \operatorname{arcsinh}(t/r_2) = 1.001$ . A torque amplitude of 10.6 Nm is predicted by (14). A finite element simulation gives 10.65 Nm. There the driving disc was 35% larger than the driven disc ( $r_2 = 90.5$  mm). If both driving disc and driven disc have  $r_2 = 67$  mm a calculation according to chapter 4.7 of [33] predicts 8.65 Nm and the analytical approximation (10b) gives only a 2% larger value with significantly less computational effort: 8.82 Nm.

## 7. CONCLUSION

The torque between two coaxial discs with multi-polar magnetization in axial direction was discussed. Starting point was the field generated by a driving disc with infinite diameter. The radial component of this field can be expressed in an exact manner as a single integral (6). It has a maximum at some specific radial distance (Fig. 2) and its dependence versus rotational position is non-sinusoidal for sufficiently small values of  $p \operatorname{arcsinh}(t/r)$  and  $p \operatorname{arcsinh}(g/r)$  (Fig. A1). The torque between an infinitely large driving disc and a finite driven disc (with diameter  $2r_2$ ) can be expressed rigorously as an integral over a term that is proportional to the radial field component (5). Also for the torque we could identify a region in the  $(p \operatorname{arcsinh}(g/r_2); p \operatorname{arcsinh}(t/r_2))$ -diagram, where its dependence on twist angle between both discs shows overshoot (Fig. 9). For a given geometry  $(g, t, r_2)$  the torque shows a maximum versus the number of pole-pairs  $p$ . These sets of parameters are located on the optimum- $p$  curve in the  $(p \operatorname{arcsinh}(g/r_2); p \operatorname{arcsinh}(t/r_2))$ -diagram (Fig. 10). The ratio of torque over volume of the magnet has a global maximum (20), which is located on the optimum- $p$  curve (Fig. 13). An upper limit for the torque on a disc with 10 cm diameter was found to be 135 Nm. To this end the discs must be infinitely thick, their axial distance must vanish, and anisotropic NdFeB magnets with  $B_{\text{rem}} = 1.32T$  are necessary (18). More economic couplings with maximum torque-volume ratio have 5.4 times smaller torque and their magnet thickness must be 27% larger than the spacing between them (21).

Comparison with numerical computations suggests that the assumption of an infinitely large driving disc seems to hold well as long as the radius of the driving disc is larger than the one of the driven disc plus the sum of spacing and thickness (Fig. 14). If both discs are equal in size one may resort to a correction term (10a). For practical cases near the optimum torque-volume ratio this procedure over-estimates the torque only by a small amount (Fig. 8).

In many practical cases one or both multi-pole magnetic rings are glued to ferromagnetic backplanes, which increase the torque and the dimensional stability of the coupling (cf. [30, 31]). The presented theory does not account for this, yet it is possible to upgrade it by use of the method of images in case of a single ferrous backplane or by use of infinite series of images between two backplanes [32, 33]. For backplanes with  $\mu_r \rightarrow \infty$  the  $B_r$ -field vanishes at its surface  $z = g + 3t/2$ , which makes the torque formula (5) more compact. This leads to curves similar to Fig. 13 yet with a different scale: Optimum systems with ferrous backplanes have thinner magnets for the same gap. This is also affirmed by the 2D approximation (25) in [30]: It leads to a torque-volume ratio of

$$\frac{\hat{T}^{(no)}}{V} = \frac{B_{rem}^2 r_2}{\mu_0 \pi^2 g} \frac{8}{3} \frac{pg/r_2}{pt/r_2} \frac{(\sinh(2pt/r_2))^2}{\sinh(4pt/r_2 + 2pg/r_2)} \quad (23)$$

The largest value of (23) is obtained for  $pt/r_2 = 0.301308$  and  $pg/r_2 = 0.487383$ . It is 2.265 times larger than the torque-volume ratio of (20a) without backplanes. Fig. 15 summarizes all properties of (23) in the  $(p \operatorname{arcsinh}(g/r_2); p \operatorname{arcsinh}(t/r_2))$ -diagram.

For practical applications it is also important to consider the significant axial force between the two discs. This is studied, e.g., in [24, 30, 33, 34] and there it is shown that the force is maximum at zero torque and vice versa. This can be used to convert a rotation into an axial vibration (e.g., for dynamic vibration absorbers or for a lock that is opened by a magnetic key).

## APPENDIX A.

When the test point approaches the driving disc the  $B_r$ - and  $B_z$ -field components versus angular position differ significantly from sinusoidal: First the maxima get flat and the patterns become similar to pulse shaped — then peaking occurs at the rising and falling edges of the pulses. This so called overshoot is studied here.

A necessary condition for the occurrence of overshoot is

$$\begin{aligned} \frac{\partial^2}{\partial \psi^2} B_r \left( r, \psi = \frac{\pi}{p}, z \right) &= 0 \\ \Rightarrow \int_{\beta=p \operatorname{arcsinh}((z-t/2)/r)}^{p \operatorname{arcsinh}((z+t/2)/r)} \frac{\sinh(\beta/p)}{\cosh \beta} \left( 1 - \frac{2}{(\cosh \beta)^2} \right) d\beta &= 0. \quad (A1) \end{aligned}$$

With  $z = t/2 + g$ ,  $\gamma = g/r$  and  $\tau = t/r$  this gives

$$\int_{\beta=p \operatorname{arcsinh}\gamma}^{p \operatorname{arcsinh}(\gamma+\tau)} \frac{\sinh(\beta/p)}{\cosh\beta} \left(1 - \frac{2}{(\cosh\beta)^2}\right) d\beta = 0 \quad (\text{A2})$$

Note that in the context of fields (not torque)  $g$  means the distance of the test point from the surface of the disc and not the gap between driving disc and driven disc. Equation (A2) defines a curve in the  $(p \operatorname{arcsinh}\gamma; p \operatorname{arcsinh}\tau)$ -plane. In the limit of vanishing thickness  $t \rightarrow 0$  the integrand must vanish and there again the second factor must vanish. It follows

$$(\cosh(p \operatorname{arcsinh}\gamma))^2 = 2 \quad \Leftrightarrow \quad p \operatorname{arcsinh}\gamma = \operatorname{arcsinh}(1) \quad (\text{A3})$$

A comparison of (A3) with Fig. 4 and (15a) in [1] shows that for  $t \rightarrow 0$  overshoot in  $B_r(\psi)$ - and  $B_z(\psi)$ -pattern occur simultaneously. It also shows that for finite  $p$  the  $(p \operatorname{arcsinh}\gamma; p \operatorname{arcsinh}\tau)$ -plane is more appropriate than the  $(p\gamma; p\tau)$ -plane, which was used in [1].

For arbitrary thickness and  $p \rightarrow \infty$  we may replace  $\sinh(\beta/p) \rightarrow \beta/p$  in (A2). Closed integration gives

$$\begin{aligned} & \frac{1 + p (\operatorname{arcsinh}\gamma) \tanh(p \operatorname{arcsinh}\gamma)}{\cosh(p \operatorname{arcsinh}\gamma)} \\ &= \frac{1 + p (\operatorname{arcsinh}\gamma + \operatorname{arcsinh}\tau) \tanh(p \operatorname{arcsinh}\gamma + p \operatorname{arcsinh}\tau)}{\cosh(p \operatorname{arcsinh}\gamma + p \operatorname{arcsinh}\tau)} \end{aligned} \quad (\text{A4})$$

For arbitrary thickness and  $p = 1$  closed integration gives

$$\frac{2}{1 + (\gamma + \tau)^2} - \frac{2}{1 + \gamma^2} = \ln \frac{1 + \gamma^2}{1 + (\gamma + \tau)^2}. \quad (\text{A5})$$

(A4) and (A5) define two overshoot-limit curves for  $p = 1$  and  $p \rightarrow \infty$ : The curves for all other values of  $p$  are between these two curves (cf. Fig. A1). Numerical values are given in Table A1.

**Table A1.** solution of (A4, A5): The table gives values for  $p \operatorname{arcsinh}\tau$  for several values of  $p \operatorname{arcsinh}\gamma$  for the extreme values  $p = 1$  and  $p \rightarrow \infty$  (the solutions for all other  $p$  are between these two extremes, cf. Fig. A1). The case  $p \operatorname{arcsinh}\tau = 0$  agrees with (15) in [1].

$p \operatorname{arcsinh}\gamma$	0.0	0.2	0.4	0.6	0.75	0.881374
$p = 1$	1.43479	1.29988	1.064080	0.710366	0.358582	0
$p \rightarrow \infty$	1.50553	1.25810	0.930983	0.556529	0.261790	0

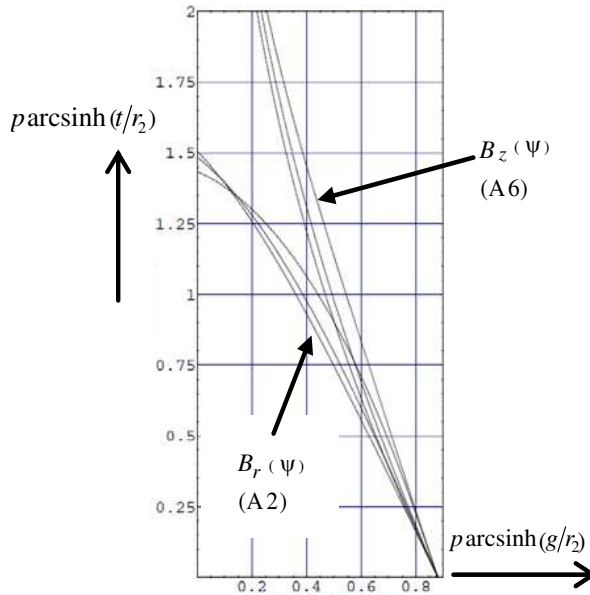


**Figure A1.** Overshoot limit curves for  $B_r(\psi)$ - and  $B_z(\psi)$ -field patterns (drawn for  $p = 1, 2, \infty$ ). For thin discs  $\text{parcsinh}(t/r_2) \rightarrow 0$  they are identical yet for thick discs they differ. For  $\text{parcsinh}(t/r_2) > 1.50553$   $B_r(\psi)$  has no overshoot whereas  $B_z(\psi)$  has overshoot if  $\text{parcsinh}(g/r_2)$  is small enough. See numerical values in Tables 5 and 6.

According to (15a) in [1] the overshoot-limit curves for the  $B_z(\psi)$  component are solutions to the equation.

$$\sinh(\text{parcsinh}(\gamma + \tau)) \sinh(\text{parcsinh}\gamma) = 1 \tag{A6}$$

For  $\gamma \rightarrow 0$  one obtains  $\tau \rightarrow \infty$ . Thus, for  $t > 0$  these limit curves are quite different from the  $B_r(\psi)$ -limit curves as is shown in Fig. A1. Numerical values are given in Table A2. For  $p = 1$  (A6) gives  $\tau = 1/\gamma - \gamma$  and for  $p \rightarrow \infty$  (A6) gives  $\text{parcsinh}\tau = \text{arcsinh}(1/\sinh(\text{parcsinh}\gamma)) - \text{parcsinh}\gamma$ .

### APPENDIX B.

Here we prove that the torque correction term (10a), accounting for the finite diameter of the driving disc, vanishes in the limit  $p \rightarrow \infty$ .

**Table A2.** Solution of (A6): The table gives values for  $\text{parcsinh}\gamma$  for several values of  $\text{parcsinh}\tau$  for the extreme values  $p = 1$  and  $p \rightarrow \infty$  (the solutions for all other  $p$  are between these two extremes, cf. Fig. A1). The case  $\text{parcsinh}\tau = 0$  agrees with (15a) in [1].

$\text{parcsinh}\tau$	0.0	1.0	2.0	3.0	4.0	$\infty$
$p = 1$	0.881374	0.584227	0.40320	0.298331	0.233929	0
$p \rightarrow \infty$	0.881374	0.468803	0.218425	0.090978	0.035362	0

First we split the integral in two positive parts

$$\begin{aligned} & \int_{\rho=0}^1 (1-\rho^2) K_0 \left( p\sqrt{(\rho-1)^2 + \gamma^2} \right) d\rho \\ &= \int_{\rho=0}^{1-\gamma} (1-\rho^2) K_0 \left( p\sqrt{(\rho-1)^2 + \gamma^2} \right) d\rho + \int_{\rho=1-\gamma}^1 (1-\rho^2) K_0 \left( p\sqrt{(\rho-1)^2 + \gamma^2} \right) d\rho \end{aligned} \quad (\text{B1})$$

where we consider only  $n = 0$ . For  $0 \leq \gamma \leq 1$  the first part is bounded by

$$\begin{aligned} & \int_{\rho=0}^{1-\gamma} (1-\rho^2) K_0 \left( p\sqrt{(\rho-1)^2 + \gamma^2} \right) d\rho < \int_{\rho=0}^{1-\gamma} 2(1-\rho) K_0(p(1-\rho)) d\rho \\ &= \frac{2}{p} (\gamma K_1(p\gamma) - K_1(p)) \end{aligned} \quad (\text{B2})$$

where we used  $1 - \rho^2 = (1 + \rho)(1 - \rho) < 2(1 - \rho)$  and  $K_0 \left( p\sqrt{(\rho-1)^2 + \gamma^2} \right) < K_0 \left( p\sqrt{(\rho-1)^2} \right)$ . For  $0 \leq \gamma \leq 1$  also the second part is bounded by

$$\begin{aligned} & \int_{\rho=1-\gamma}^1 (1-\rho^2) K_0 \left( p\sqrt{(\rho-1)^2 + \gamma^2} \right) d\rho \\ & < \int_{\rho=1-\gamma}^1 2\gamma K_0 \left( p\sqrt{2}(\rho-1) \right) d\rho = 2\gamma^2 K_0 \left( p\sqrt{2}(\varepsilon\gamma) \right) \end{aligned} \quad (\text{B3})$$

Here we used  $K_0 \left( p\sqrt{(\rho-1)^2 + \gamma^2} \right) < K_0 \left( p\sqrt{(\rho-1)^2 + (\rho-1)^2} \right)$ .

The integration was not carried out because it leads to the Struve

function  $L_{-1}(0)$  (which is not defined at zero and we would therefore need to use a limit approach). Instead we used the mean value theorem for integrals according to which the last identity in (B3) is valid for some  $\varepsilon$  with  $0 \leq \varepsilon \leq 1$ .

In (10) the integral of (B1) is multiplied by  $p$

$$\begin{aligned}
 & p \int_{\rho=0}^1 (1 - \rho^2) K_0 \left( p \sqrt{(\rho - 1)^2 + \gamma^2} \right) d\rho \\
 & < 2\gamma K_1(p\gamma) - 2K_1(p) + 2\gamma(p\gamma) K_0 \left( \varepsilon p \gamma \sqrt{2} \right) \quad (B4)
 \end{aligned}$$

In the limit  $p \rightarrow \infty$  with  $p\gamma$  remaining finite this means  $\gamma \rightarrow 0$  and therefore all terms in (B4) vanish. We can repeat this argument with the other two terms in the integrand of (10) by using  $\gamma + \tau$  and  $\gamma + 2\tau$  instead of  $\gamma$ . This holds also for  $n > 0$ . Therefore, (10) vanishes for  $p \rightarrow \infty$ . This shows that our theory is accurate for two cases: (i) for arbitrary  $p$  and infinite  $r_2$ , and (ii) for infinite  $p$  and arbitrary  $r_2$ .

### APPENDIX C.

Here we prove a transformation of the torque integral, which is used several times throughout this paper. Inserting (6) into (5) gives

$$\begin{aligned}
 T(\psi_0) = & \frac{2pB_{\text{rem}}^2 r_2^3}{\mu_0 \pi} \sin(p\psi_0) \int_{\rho=0}^1 (1 - \rho^2) \left\{ \int_{\beta=p \operatorname{arcsinh}((\gamma+\tau)/\rho)}^{p \operatorname{arcsinh}((\gamma+2\tau)/\rho)} \right. \\
 & \left. \frac{\sinh(\beta/p) \cosh \beta}{(\cosh \beta)^2 - (\cos(p\psi))^2} d\beta - \int_{\beta=p \operatorname{arcsinh}(\gamma/\rho)}^{p \operatorname{arcsinh}((\gamma+\tau)/\rho)} \frac{\sinh(\beta/p) \cosh \beta}{(\cosh \beta)^2 - (\cos(p\psi))^2} d\beta \right\} d\rho \quad (C1)
 \end{aligned}$$

In Sections 4, 5, and 6 several properties of the torque are discussed and it is found that they are located in the finite area  $0 < p \operatorname{arcsinh} \gamma < 2$  and  $0 < p \operatorname{arcsinh} \tau < 4$  in the  $(p \operatorname{arcsinh} \gamma; p \operatorname{arcsinh} \tau)$ -plane. This implies that in the limit  $p \rightarrow \infty$  it must hold  $\gamma \rightarrow 0$  and  $\tau \rightarrow 0$ . Therefore one is allowed to use  $p \operatorname{arcsinh} \gamma \rightarrow p\gamma$  and  $p \operatorname{arcsinh} \tau \rightarrow p\tau$ . However, this is no justification to use  $p \operatorname{arcsinh}(\gamma/\rho) \rightarrow p\gamma/\rho$  in (C1), because the integration variable  $\rho$  also assumes zero! Yet, we may

write for the second integral in (C1)

$$\begin{aligned}
& \lim_{p \rightarrow \infty} \int_{\rho=0}^1 \int_{\beta=\text{parcsinh}(\gamma/\rho)}^{\text{parcsinh}((\gamma+\tau)/\rho)} \frac{(1-\rho^2) \sinh(\beta/p) \cosh \beta}{(\cosh \beta)^2 - (\cos(p\psi_0))^2} d\beta d\rho \\
&= \lim_{p \rightarrow \infty} \left\{ \int_{\beta=\text{parcsinh}(\gamma+\tau)}^{\infty} \int_{\rho=\gamma/\sinh(\beta/p)}^{(\gamma+\tau)/\sinh(\beta/p)} \frac{(1-\rho^2) \sinh(\beta/p) \cosh \beta}{(\cosh \beta)^2 - (\cos(p\psi_0))^2} d\beta d\rho \right. \\
&+ \left. \int_{\beta=\text{parcsinh} \gamma}^{\text{parcsinh}(\gamma+\tau)} \int_{\rho=\gamma/\sinh(\beta/p)}^1 \frac{(1-\rho^2) \sinh(\beta/p) \cosh \beta}{(\cosh \beta)^2 - (\cos(p\psi_0))^2} d\beta d\rho \right\} \\
&= \int_{\beta=p(\gamma+\tau)}^{\infty} \int_{\rho=p\gamma/\beta}^{p(\gamma+\tau)/\beta} \frac{(1-\rho^2) (\beta/p) \cosh \beta}{(\cosh \beta)^2 - (\cos(p\psi_0))^2} d\beta d\rho \\
&+ \int_{\beta=p\gamma}^{p(\gamma+\tau)} \int_{\rho=p\gamma/\beta}^1 \frac{(1-\rho^2) (\beta/p) \cosh \beta}{(\cosh \beta)^2 - (\cos(p\psi_0))^2} d\beta d\rho \\
&= \int_{\rho=0}^1 \int_{\beta=p\gamma/\rho}^{p(\gamma+\tau)/\rho} \frac{(1-\rho^2) (\beta/p) \cosh \beta}{(\cosh \beta)^2 - (\cos(p\psi_0))^2} d\beta d\rho \tag{C2}
\end{aligned}$$

This is the justification to skip the arcsinh-functions in (C1). It follows

$$\begin{aligned}
\lim_{p \rightarrow \infty} T(\psi_0) &= \frac{2pB_{\text{rem}}^2 r_2^3}{\mu_0 \pi p} \int_{\rho=0}^1 (1-\rho^2) \left\{ \int_{\beta=p(\gamma+\tau)/\rho}^{p(\gamma+2\tau)/\rho} \right. \\
&\quad \left. \frac{\sin(p\psi_0) \beta \cosh \beta}{(\cosh \beta)^2 - (\cos(p\psi_0))^2} d\beta - \int_{\beta=p\gamma/\rho}^{p(\gamma+\tau)/\rho} \frac{\sin(p\psi_0) \beta \cosh \beta}{(\cosh \beta)^2 - (\cos(p\psi_0))^2} d\beta \right\} d\rho \tag{C3}
\end{aligned}$$

## REFERENCES

1. Ausserlechner, U., "Closed analytical formulae for multi-pole magnetic rings," *Progress In Electromagnetics Research B*, Vol. 38, 71–105, 2012.

2. Bancel, F. and G. Lemarquand, "Three-dimensional analytical optimization of permanent magnets alternated structure," *IEEE Trans. Magn.*, Vol. 34, No. 1, 242–247, Jan. 1998.
3. Bancel, F., "Magnetic nodes," *J. Phys. D: Appl. Phys.*, Vol. 32, 2155–2161, 1999.
4. Liu, W. Z., C. Y. Xu, and Z. Y. Ren, "Research of the surface magnetic field of multi-pole magnetic drum of magnetic encoder," *Int'l Conf. Sensors and Control Techniques, Proceedings of SPIE*, D.-S. Jiang and A.-B. Wang, editors, Vol. 4077, 288–291, 2000.
5. Furlani, E. P., "A three-dimensional field solution for axially-polarized multipole discs," *J. Magn. Magn. Mat.*, Vol. 135, 205–214, 1994.
6. Ravaut, R. and G. Lemarquand, "Magnetic field created by a uniformly magnetized tile permanent magnet," *Progress In Electromagnetics Research B*, Vol. 24, 17–32, 2010.
7. Ravaut, R., G. Lemarquand, V. Lemarquand, and C. Depollier, "Magnetic field produced by a tile permanent magnet whose polarization is both uniform and tangential," *Progress In Electromagnetics Research B*, Vol. 13, 1–20, 2009.
8. Ravaut, R. and G. Lemarquand, "Analytical expression of the magnetic field created by tile permanent magnets tangentially magnetized and radial currents in massive disks," *Progress In Electromagnetics Research B*, Vol. 13, 309–328, 2009.
9. Nihei, H., "Analytic expressions of magnetic multipole field generated by a row of permanent magnets," *Jap. J. Appl. Phys.*, Vol. 29, No. 9, 1831–1832, Sept. 1990.
10. Ozeretskovskiy, V., "Calculation of two-dimensional nonperiodic multipole magnetic systems," *Sov. J. Commun. Techn. and Electr.*, Vol. 36, No. 8, 81–92, Aug. 1991.
11. Grinberg, E., "On determination of properties of some potential fields," *Applied Magnetohydrodynamics*, Reports of the Physics Inst. Riga, Vol. 12, 147–154, 1961.
12. Avilov, V. V., "Electric and magnetic fields for the riga plate," Internal Report FZR Forschungszentrum Rossendorf, Dresden, Germany, 1998. Published in a report by E. Kneisel, "Numerische und experimentelle untersuchungen zur grenzschichtbeeinflussung in schwach leitfähigen flüssigkeiten," Nov. 24, 2003, <http://www.hzdr.de/FWS/FWSH/Mutschke/kleinerbeleg.pdf>.
13. De Visschere, P., "An exact two-dimensional model for a periodic circular array of head-to-head permanent magnets," *J. Phys. D: Appl. Phys.*, Vol. 38, 355–362, 2005.

14. Furlani, E. P. and M. A. Knewton, "A three-dimensional field solution for permanent-magnet axial-field motors," *IEEE Trans. Magn.*, Vol. 33, No. 3, 2322–2325, May 1997.
15. Furlani, E. P., "Analytical analysis of magnetically coupled multipole cylinders," *J. Phys. D: Appl. Phys.*, Vol. 33, 28–33, 2000.
16. Ravaud, R. and G. Lemarquand, "Magnetic couplings with cylindrical and plane air gaps: Influence of the magnet polarization direction," *Progress In Electromagnetics Research B*, Vol. 16, 333–349, 2009.
17. Ravaud, R., G. Lemarquand, V. Lemarquand, and C. Depollier, "Torque in PM couplings: Comparison of uniform and radial magnetization," *J. Appl. Phys.*, Vol. 105, 053904, 2009, DOI: 10.1063/1.3074108.
18. Ravaud, R., G. Lemarquand, V. Lemarquand, and C. Depollier, "Permanent magnet couplings: Field and torque three-dimensional expressions based on the coulombian model," *IEEE Trans. Magn.*, Vol. 45, No. 4, 1950–1964, 2009.
19. Yao, Y. D., G. J. Chiou, D. R. Huang, and S. J. Wang, "Theoretical computations for the torque of magnetic coupling," *IEEE Trans. Magn.*, Vol. 31, No. 3, 1881–1884, May 1995.
20. Huang, D. R., G.-J. Chiou, Y.-D. Yao, and S.-J. Wang, "Effect of magnetization profiles on the torque of magnetic coupling," *J. Appl. Phys.*, Vol. 76, No. 10, 6862–6864, Nov. 1994.
21. Yao, Y. D., D. R. Huang, C. C. Hsieh, D. Y. Chiang, S. J. Wang, and T. F. Ying, "The radial magnetic coupling studies of perpendicular magnetic gears," *IEEE Trans. Magn.*, Vol. 32, No. 5, 5061–5063, Sept. 1996.
22. Tsamakidis, D., M. Ioannides, and G. Nicolaidis, "Torque transfer through plastic bonded Nd<sub>2</sub>Fe<sub>14</sub>B magnetic gear system," *J. Alloys Compounds*, Vol. 241, 175–179, 1996.
23. Nagrial, M. H., J. Rizk, and A. Hellany, "Design of synchronous torque couplers," *World Academy of Science, Engineering and Technology*, Vol. 79, 426–431, 2011.
24. Furlani, E. P., "Formulas for the force and torque of axial couplings," *IEEE Trans. Magn.*, Vol. 29, No. 5, 2295–2301, 1993.
25. Furlani, E. P., "Analysis and optimization of synchronous magnetic couplings," *J. Appl. Physics*, Vol. 79, No. 8, 4692–4694, 1996.
26. Furlani, E. P., "Field analysis and optimization of axial field permanent magnet motors," *IEEE Trans. Magn.*, Vol. 33, No. 5,

- 3883–3885, 1997.
27. Furlani, E. P., “Computing the field in permanent-magnet axial-field motors,” *IEEE Trans. Magn.*, Vol. 30, No. 5, 3660–3663, 1994.
  28. Furlani, E. P., “A method for predicting the field in permanent magnet axial-field motors,” *IEEE Trans. Magn.*, Vol. 28, No. 5, 2061–2066, 1992.
  29. Nagrial, M. H., “Design optimization of magnetic couplings using high energy magnets,” *Electr. Machines and Power Systems*, Vol. 21, No. 1, 115–126, 1993.
  30. Lubin, T., S. Mezani, and A. Rezzoug, “Simple analytical expressions for the force and torque of axial magnetic couplings,” *IEEE Trans. Energy Conversion*, Vol. 99, 1–11, 2012.
  31. Zheng, P., Y. Haik, M. Kilani, and C.-J. Chen, “Force and torque characteristics for magnetically driven blood pump,” *J. Magn. Magn. Mat.*, Vol. 241, 292–302, 2002.
  32. Kellog, O. D., “Electric images: Infinite series of images,” *Foundations of Potential Theory*, Chapter IX 1, 230, Dover Publications, Inc., NY, 1954, ISBN 0-486-60144-7.
  33. Furlani, E. P., “Axial-field motor,” *Permanent Magnet and Electromechanical Devices*, Chapter 5.13, Fig. 5.44, 434, Academic Press, San Diego, 2001, ISBN 0-12-269951-3.
  34. Waring, R., J. Hall, K. Pullen, and M. R. Etemad, “An investigation of face type magnetic couplers,” *Proc. Inst. Mech. Eng. A, J. Power and Energy*, Vol. 210, No. 4, 263–272, 1996.